

Transfer of olivine crystallographic orientation through a cycle of serpentinisation and dehydration

Kristina G. Dunkel^{a,1}, Håkon Austrheim^{a,2}, Benoit Ildefonse^{b,3}, and Bjørn Jamtveit^{a,4}

^a*Physics of Geological Processes (PGP), University of Oslo, P.O. Box 1048 Blindern, 0136
Oslo, Norway*

^b*Géosciences Montpellier, CNRS & Université Montpellier, 34095 Montpellier, France*

¹*kristina.dunkel@geo.uio.no, ORCID: 0000-0002-4100-381X*

²*ORCID: 0000-0002-8521-4547*

³*ORCID: 0000-0001-7635-9288*

⁴*ORCID: 0000-0001-5700-1803*

Abstract: Our ability to decipher the mechanisms behind metamorphic transformation processes depends in a major way on the extent to which crystallographic and microstructural information is transferred from one stage to another. Within the Leka Ophiolite Complex in the Central Norwegian Caledonides, prograde olivine veins that formed by dehydration of serpentinite veins in dunites exhibit a characteristic distribution of microstructures: The outer part of the veins comprises coarse-grained olivine that forms an unusual, brick-like microstructure. The inner part of the veins, surrounding a central fault, is composed of fine-grained olivine. Where the fault movement included a dilational component, optically clear, equant olivine occurs in the centre. Electron-backscatter diffraction mapping reveals that the vein olivine has inherited its crystallographic-preferred orientation (CPO) from the olivine in the porphyroclastic host rock; however misorientation is weaker and associated to different rotation axes. We propose that prograde olivine grew epitaxially on relics of mantle olivine and thereby acquired its CPO. Growth towards pre-existing microfractures along which

serpentinisation had occurred led to straight grain boundaries and a brick-like microstructure in the veins. When dehydration embrittlement induced slip, a strong strain localisation on discrete fault planes prevented distortion of the CPO due to cataclastic deformation; grain size reduction did not significantly modify the olivine CPO. This illustrates how a CPO can be preserved though an entire metamorphic cycle, including hydration, dehydration, and deformation processes, and that the CPO and the microstructures (e.g., grain shape) of one phase do not necessarily record the same event.

Keywords: deserpentinisation; EBSD; ophiolite; CPO; epitaxy

INTRODUCTION

Dehydration of serpentinites to form olivine-bearing rocks is a common process during subduction or contact metamorphism of previously hydrated ultramafic rocks. Depending on pressure, temperature, and chemical composition, serpentine minerals (and brucite) break down to olivine (and talc or enstatite) and water. The released fluids play an important role in global geochemical cycles (e.g., Deschamps et al. 2013), may lead to secondary hydration of neighbouring lithologies (e.g., Hyndman and Peacock 2003), and trigger melting of the mantle wedge above subducting slabs, resulting in arc magmatism (e.g., Kay 1980; Rüpke et al. 2004). They have also been suggested to cause embrittlement in the dehydrating rocks (e.g., Hacker et al. 2003; Raleigh and Paterson 1965) or their surroundings (Rutter et al. 2009), potentially inducing intermediate-depth earthquakes in subduction zones (e.g., Jung et al. 2004; Shiina et al. 2013; Yamasaki and Seno 2003).

Two main types of olivine-bearing rocks produced by serpentine dehydration are described in the literature: veins within large serpentinite bodies (e.g., Healy et al. 2009; Scambelluri et al. 1991; Vance and Dungan 1977) and prograde peridotites with sharp

boundaries towards the original serpentinite (e.g., Jabaloy-Sánchez et al. 2015; Padrón-Navarta et al. 2011). Olivine morphology ranges from small, irregular grains in veins (Plümper et al. 2017) or around serpentinitised primary olivine (e.g., Debret et al. 2013a; Debret et al. 2013b) to spinifex-like “jackstraw” olivine (Snoke and Calk 1978). In most of these examples, the ultramafic rocks were completely serpentinitised before dehydration started. In situations where the initial degree of serpentinitisation is low and serpentinitisation is concentrated along fractures or subgrain boundaries (e.g., Plümper et al. 2012a), pre-existing structures and the pattern of serpentinitisation are potential influences on the morphology and orientation of the prograde olivine.

In the following, we describe olivine veins in dunites from the Leka Ophiolite Complex (LOC), Norway. They represent dehydrated serpentinite veins, and experienced grain size reduction due to dehydration embrittlement in an advanced stage of deserpentinitisation (Dunkel et al. 2017). Here, we use electron backscatter diffraction (EBSD) mapping to characterise the microstructures of the veins and their evolution during dehydration and faulting.

GEOLOGICAL SETTING

Regional geology

The Leka Ophiolite Complex crops out on the island of Leka in Nord-Trøndelag, Norway (Fig. 1a) and represents part of the Upper or Uppermost Allochthon of the Norwegian tectonostratigraphy. The ophiolite was dated at 497 ± 2 Ma (Dunning and Pedersen 1988) and formed in a supra-subduction zone setting of the North Iapetus Ocean (Furnes et al. 1988). A dehydration event was proposed for the LOC based on olivine pseudomorphs after serpentinitised orthopyroxene in the mantle tectonites (Plümper et al. 2012b). It was probably the same dehydration event that determined the radiogenic and stable isotope compositions of

talc-carbonate alteration products in the ultramafic cumulates (Bjerga et al. 2015). The exact timing and cause of the dehydration event are unknown, but the geological setting makes a classical subduction-related deserpentinisation unlikely. See Plümper et al. (2012b) for a discussion of possible dehydration scenarios.

Formation and deformation of prograde olivine veins in the LOC

Dunites from the lower part of the ultramafic cumulates of the LOC contain olivine veins. The rocks are devoid of a macroscopically visible foliation or lineation, but a microscopic lineation can be inferred from EBSD data (see *Crystallographic preferred orientations*). The olivine veins are interpreted to have formed by dehydration of serpentinite veins based on their heterogeneous, Fe-poor compositions, their abundance of magnetite inclusions, and their oxygen isotope ratios (Dunkel et al. 2017). The pre-existing serpentinite veins (as opposed to veins of pure serpentine) were partly serpentinitised regions centred on a fracture. Accordingly, the term “veins” in the following refers to replacement veins, in contrast to the common definition of veins which excludes replacement and limits veins to mineral aggregates precipitated in dilation sites (e.g., Bons et al. 2012).

During prograde metamorphism, serpentine was dehydrated to olivine, and the fluid pressure increased, which led to dehydration embrittlement, slip in the vein centres, and a pulverization of the prograde olivine adjacent to the slip plane (Dunkel et al. 2017). Microstructural evidence of this process includes the sharp displacement of chromite layers along faults in the vein centres (Fig. 1b, c), and a pronounced grain size decrease from the outer to the inner part of the veins.

The veins are oriented in two subperpendicular sets (Fig. 1d), one striking approximately E-W with a vertical dip, the other one striking approximately N-S and dipping ca. 40° to the east. Faults are located in the centres of the E-W striking veins. A mm- to dm-

scale displacement is recorded by chromite layers in dunite, which strike approximately N-S (009, 50 E in the sampled area, Fig. 1d). Due to the lack of markers in the other direction, the amount of displacement is unclear in the N-S striking veins. However the microstructures of the two vein sets are indistinguishable.

Four microstructural domains are defined on the basis of colour in the field and olivine microstructures (Fig. 2a-c; Dunkel et al. 2017). The dunitic host (domain A) is cross-cut by prograde olivine with heterogeneous compositions and magnetite inclusions in the outer parts of the veins (domain B) and fine-grained prograde olivine in the inner parts of the veins (domain C). Domain D, comprising optically clear equant olivine, occurs in areas that experienced local dilation in the central fault zone, and has been observed in seven of the ten analysed veins. Domains A to C are replacement veins, while domain D is dilational. This can be inferred from the chromite layers, which are continuous throughout domains A to C and only show fault-perpendicular displacement where domain D is developed.

All microstructural domains have been affected by late lizardite and antigorite serpentinisation as described by Plümper et al. (2012b).

In this contribution, we mainly discuss the preservation of a crystallographic preferred orientation in the veins during hydration and dehydration and the formation of the prograde olivine microstructures. Formation of the veins themselves and faulting and pulverisation of olivine caused by dehydration embrittlement are documented and discussed in Dunkel et al. (2017).

METHODS

As no foliation or lineation is visible in the field or in hand specimens, thin sections were made parallel to the outcrop surface to allow for easy comparison of macro- and microstructures.

Crystallographic orientations of olivine, antigorite, chromite, and magnetite were determined by indexing of electron-backscatter diffraction patterns using the CamScan X500FE Crystal Probe at Geosciences Montpellier (CNRS-Université de Montpellier, France), equipped with an Oxford/Nordlys EBSD detector. The Crystal Probe was used at an accelerating voltage of 20 kV, and a working distance of 25 mm. The step size used for EBSD mapping varied between 0.5 μm (for the investigation of grain internal structures) and 15 μm (to determine preferred orientations). EBSD patterns were indexed automatically using the AZtec software from Oxford Instruments. Because of the similar crystallographic structures of chromite and magnetite, automatic indexing of these two minerals was problematic. Therefore, the intensity ratios of qualitative energy-dispersive spectrometry (EDS) element maps of Cr and Fe, which were acquired concurrently to the EBSD maps, were used to distinguish chromite and magnetite using the Tango software of the Channel 5® suite (HKL Technology).

The amount of non-indexed pixels (5-20 %) is only a few percent points higher than the amount of lizardite or chrysotile in the respective area (as estimated from image analysis of backscatter electron images), hence inferred to be essentially related to these phases. Despite the high indexation rates, post-acquisition data processing was done using the Tango software of the Channel 5® suite (HKL Technology), to remove small not-indexed areas within larger grains, and to correct for systematic misindexing. It consists of (i) removing isolated pixels that are indexed as a given phase and surrounded by either non-indexed pixels or pixels indexed for another phase, (ii) filling non-indexed pixels that have a minimum of 6 neighbouring pixels with the same orientation, and (iii) correcting systematic misindexing errors due to the olivine hexagonal pseudo-symmetry around [100].

Further analysis and visualisation of the crystallographic orientations has been

conducted using the Matlab toolbox MTEX (version 4.3.1; <http://mtex-toolbox.github.io>; Bachmann et al. 2010; Bachmann et al. 2011; Hielscher and Schaeben 2008). A misorientation threshold of 10° was used for grain modelling. Grains smaller than or equal to 2 pixels were excluded for all analyses. For grain size determinations, only grains containing 10 pixels or more were considered. Non-indexed pixels have been included in the grains to reconstruct the grain distribution before the fragmentation of olivine grains by late serpentine veins. Orientation distribution functions (e.g., Mainprice et al. 2014) characterising olivine crystallographic preferred orientations (CPO) were computed using average grain orientations instead of individual data points to avoid over-representation of the larger grains, because microstructures and not physical properties were the focus of this study.

In the absence of a visible foliation or lineation, all pole figures are oriented perpendicular to the chromite layering (inferred to be parallel to the foliation). The shape-preferred orientation of olivine in domain A (presumably parallel to the lineation) is subparallel to the mean [100] orientation as described below (*Crystallographic preferred orientations*).

The strength of a CPO can be defined by two dimensionless indices, the J index (texture index), and the M index (misorientation index). The J index is the volume-averaged integral of the squared orientation densities and ranges between 1 (for a random distribution) and infinity (for a single crystal) (Bunge 1982; Mainprice et al. 2014; Mainprice and Silver 1993). The M index is defined as the difference between the observed distribution of uncorrelated misorientation angles and that for a random fabric (Mainprice et al. 2014; Skemer et al. 2005) and ranges between 0 (random) and 1 (single crystal). Both are calculated using MTEX. The orientation distribution functions from which these indices are calculated were computed with a fixed half-width of the de la Vallee Poussin kernel (10°), as

recommended by Mainprice et al. (2014).

RESULTS

Microstructures

EBSD data has been acquired in two samples taken approximately 20 cm from each other (Fig. 1d-f). Optical micrographs and phase maps (Figs 2a-c, 3a) highlight the differences between the four microstructural domains described above (*Formation and deformation of prograde olivine veins in the LOC*). Additional micrographs showing similar microstructures in a clearly displacive setting are shown in Online Resource 1. Olivine in domain B is coarser-grained than that in domains A and C and domain C has a more homogeneous grain size than domain A (Figs 2a-c, 3). Quantifying the grain sizes is difficult as the grain size distributions do not show a clear maximum, so that the modal or mean grain sizes are not very meaningful (see Online Resource 2 for the three-dimensional grain size distributions calculated using the method described by Lopez-Sanchez and Llana-Fúnez, 2015, and Lopez-Sanchez, 2016) and standard deviations are large. Nevertheless we present some approximate values in the following (see also table 1). Grain sizes are given as equivalent diameters, i.e., the diameters of circles having the same area as the respective grains. It should be noted that different step sizes were used for some of the areas, which may influence the grain size measurements. In some areas, late serpentine has fragmented olivine grains to such a degree that they could not be reconstructed adequately during grain modelling, skewing the results to lower average grain sizes. By weighing the average grain diameter by the grain area, the influence of those small grains is reduced.

Olivine in domain A has a mean equivalent diameter of 68 μm (area-weighted: 119 μm). Rare porphyroclasts (Fig. 2c) can reach several millimetres in diameter, and have a shape-preferred orientation subparallel to the lithological layering. Some show undulose

extinction, but most have sharp, parallel subgrain boundaries.

Domain B consists of larger olivines with a mean equivalent diameter of 127 μm (area-weighted: 413 μm). Many of the grains have very straight grain boundaries, which extend over several neighbouring grains (Fig. 3a), giving the microstructure a brick-like appearance. These continuous planar features are particularly common parallel to the orientation of the veins. Where they hit chromite grains, the chromite is usually fractured, but the fragments are not displaced relative to each other. Olivines in domain B do not show microstructural evidence of plastic deformation such as clear subgrain boundaries or undulose extinction. Next to domain A, the long axes of many olivine grains in domain B are perpendicular to the boundary between the two domains, thus defining a palisade-type microstructure (Figs 2c, 3). The limited size of the palisade-like part of domain B and the intermediate characteristics, between those of domains B and A, make it difficult to isolate this part; it is therefore not treated separately in the following. The A-B boundary may pass through single optically continuous crystals of olivine, with abundant magnetite inclusions being present in the B-part (Fig. 2d).

Domain C has an appearance similar to A, with a mean equivalent diameter of 61 μm (area-weighted: 112 μm). Aggregates of small olivine grains with similar crystallographic orientation (CPO-domains) are commonly visible in orientation maps (Fig. 3b). Some of these CPO-domains show a weak shape-preferred orientation coinciding with the large-scale displacement direction as recorded by the offset chromite layers. Faults occur in the centre of domain C or at the border between domains C and D, as evidenced by cut chromite grains (Fig. 2e).

The grain size of olivine occurring in the centre of some veins (domain D) varies between different samples, but is relatively homogeneous within each one. No discrete values

are given because of the paucity of data from this domain.

Crystallographic preferred orientations

An olivine CPO with a constant direction is observed for all domains (Fig. 4). [100] is oriented preferentially parallel to the traces of the chromite layers (i.e., to the lithological layering). The J and M indices point to weak fabrics for all domains (Tab. 2), with values between 1.54 and 1.84 for J and 0.05 and 0.09 for M, for domains A to C. The intensity of the CPO seems to increase from domain A over B to C (Fig. 4); however the small differences between these relatively weak fabric intensities may not be significant. In one sample, domain D has the highest of all fabric indices (J=3.91, M=0.09), but this is a likely bias due to the much smaller number of measured grains.

The fabric strength of individual pole figures (pfJ) decreases from [100] over [010] to [001] in all but one analysed area (Fig. 4, Tab. 2), indicating a prolate fabric dominated by the lineation.

Misorientations

Porphyroclasts in domain A display the strongest misorientations (expressed as the angle between each pixel orientation and the mean grain orientation) and parallel subgrain boundaries (Fig. 5a). Misorientation in olivines in domains B and D is weaker (usually below 5°) and the subgrain distribution is patchy (Fig. 5b, d). The subgrain arrangement in domain C olivines is similar to that in B and D, but the misorientations can be as high as in A (Fig. 5c).

In domain A, misorientations appear to be crystallographically controlled. Inverse pole figures of the rotation axes for 2 to 10° misorientations between adjacent pixels show a maximum around [010], and a minor contribution of [001] (Fig. 6). The distributions of rotation axes in domains B, C, and D are almost random. While there are maxima in the rotation axes, they are different from and weaker than for domain A. Exceptions to this are

domains B and C in sample LE05-14, which have misorientation rotation axes similar to domain A.

DISCUSSION

Formation of the primary olivine CPO by crystal plastic deformation

In domain A, the relative strength of the [100] distribution compared to the other axes and the concentration of low-angle misorientation rotation axes around [010] and, subordinately, [001] are consistent with a fabric formed by dislocation glide on the {0kl}[100] system or by a combination of (010)[100] and (001)[100]. Whether slip on (010) or (001) was more active cannot be determined. The generally higher pfJ indices for [010] than for [001] would indicate that (010) is the dominant slip plane, while the preference for [010] over [001] as the low-angle misorientation axis would suggest that (001)[100] dominates over (010)[100]. In general, the {0kl}[100] slip systems are active at deformation temperatures of ca. 1000 °C (e.g., Carter and Ave'Lallemant 1970; Nicolas and Christensen 1987; Tommasi et al. 2000, and references therein). Which slip system is active also depends on the water content of olivine: Deformation along (010)[100], at low water contents, leads to an A-type olivine fabric, while deformation along (001)[100], at water contents above ca. 200 ppm H/Si, leads to an E-type fabric (Katayama, et al. 2004). The stress is in both cases below ca. 350 MPa (Jung, et al. 2006). The orientation of the maxima in the pole figures supports an A-type fabric, however as stated above the orientation of foliation and lineation is uncertain.

The parallelism of magmatic layering and [100] orientation indicates that the crystal-plastic deformation is a primary feature and unrelated to the veins. It could also mean that a preferred orientation already developed during crystal settling, but the distribution of misorientation rotation axes clearly indicates that deformation was active.

Preservation of the olivine CPO during hydration and dehydration

While the olivine CPO is the same in domains A and B, misorientation is lower in B and the distribution of low-angle misorientation rotation axes is almost random; the rotations are less crystallographically controlled. This shows that two different mechanisms operated in the two domains. Crystal-plastic deformation as observed in domain A is unlikely to be localised on the microscale, and could not have affected only the host rock. Thus, crystal-plastic deformation occurred before the hydration and dehydration stages, during which grain size, chemistry, and misorientation changed but the CPO was preserved.

After a high-temperature deformation event produced a homogeneous fabric in the whole rock (i.e., everything once looked like domain A looks today), large-scale fracturing allowed for fluid infiltration at lower temperatures. In alteration zones around the fractures, olivine reacted to serpentine and magnetite (and probably brucite). When serpentine (and brucite) broke down at higher temperatures, prograde olivine with the same CPO as the primary olivine formed. In the absence of relict serpentine from this stage, which serpentine polymorph initially grew cannot be determined; however antigorite is the only polymorph stable at the temperatures required to form prograde olivine.

Topotaxy between olivine and antigorite can preserve a CPO during the transition from olivine to antigorite (Boudier et al. 2010) and from antigorite to olivine (Boudier et al. 2010; Padrón-Navarta et al. 2015). A weakening of the CPO was documented by Padrón-Navarta et al. (2015) for the prograde reaction. The olivine axis that is perpendicular to the basal plane of antigorite can be strongly concentrated after dehydration, but the other two axes should be more disperse. However, we observe neither a weakening of the overall olivine CPO (there is no large change in the J and M indices) nor a concentration of one olivine axis. Therefore, the initial CPO was probably preserved by epitaxial growth of prograde olivine on

relics of primary olivine. Crystallographic continuity between olivine relics and neoblasts has been observed before in ultramafites from the Sultan-Darrington area, North Cascades, Washington (Dungan 1977) and in non-equilibrium dehydration experiments on natural serpentinites (Raleigh and Paterson 1965). This epitaxial growth is only possible if serpentinisation was incomplete, and if serpentine did not grow in large open veins, but in a mesh texture surrounding olivine relics. The alteration was limited to the immediate vicinity of fractures. This mode of serpentinisation is consistent with the lack of dilational movement in domains A to C, as shown by the absence of gaps in the chromite layers in these domains. High variations in forsterite content in single olivine crystals of domain B support the survival of relict primary olivine in the veins as well. The intensity of these chemical variations in domain B increases towards the host dunite, reflecting a decrease in the degree of serpentinisation with distance from the fractures along which fluids penetrated the rocks (Dunkel et al. 2017). The presence of relics of domain A in domain B may also be the reason for the similarity between the rotation axes distributions of domains A and B in sample LE05-14.

Formation of the prograde olivine microstructures

The brick-like microstructure is a characteristic feature of domain B. While this microstructure may appear similar to a classic crack-seal vein, the formation was different. Crack-seal veins form by repeated fracturing and mineral precipitation and are extensional features (Ramsay, 1980). In contrast, the chromite layers which are displaced along the veins described here have not moved perpendicular to the veins. Apart from domain D (see ‘Olivine growth after stress release’), the features described here are replacive.

Several other mechanisms can cause straight grain boundaries: Static grain growth in the presence of fluids has been proposed to cause the formation of tabular olivine crystals, or

olivine “tablets”, i.e., euhedral, strain-free neoblasts (e.g., Boullier and Nicolas 1975; Drury and van Roermund 1989). This would imply, however, that the planar grain boundaries correspond to olivine crystal faces, which they do not. Straight grain boundaries can also develop from subgrain boundaries. However, one of the crystallographic axes of olivine should have the same orientation on opposite sides of a straight grain boundary, which is not the case. Additionally, neither of these possibilities explains why the straight grain boundaries extend over several grains (Fig. 3a). Therefore, we posit that the straight boundaries represent pre-existing fractures. Initially, the dunite had a porphyroclastic fabric, preserved in the present-day host rock (domain A). Fracturing provided fluid pathways and initiated serpentinisation to form serpentine-rich regions around the fractures (Fig. 7a, b). No perceptible shear movement occurred at that stage, as evidenced by the chromite grains, which show little deformation in domain B and no offset along the straight olivine grain boundaries. This may suggest that thermal rather than tectonic forces caused the fracturing. During the dehydration event, olivine nucleated on relics of the primary olivine in the centres of the serpentine mesh and grew outwards towards the fractures (Fig. 7c), which were preserved as grain boundaries when dehydration was complete (Fig. 7d).

The increase in olivine grain size from domain A to domain B may be due to the availability of fluids during serpentine dehydration, which facilitated the transport of ions to the growing crystals. Because of the low permeability of the host dunite, the influence of the fluid was likely limited to the serpentinite veins. The grain size may also be strongly influenced by the amount of olivine grains present before the dehydration. Since the CPO is not weakened from domain A to domain B, the prograde olivine grew dominantly on relics of primary olivine, without significant nucleation of new grains. A low nucleation rate is consistent with deserpentinisation, which is likely to occur without large temperature

overstepping of the dehydration reaction.

The palisade-like microstructure at the border to domain A resembles elongate-blocky veins (e.g., Fisher and Brantley 1992), which are a type of syntaxial veins where crystals grow out from the wall rock and become elongated in the growth direction (e.g., Bons et al. 2012). Because the growth of olivine in this case did not occur in a dilational site, this is not directly comparable, but the growth mechanism might be similar. It is likely that most of the prograde olivine nucleated on the vein walls and grew inwards, even though it did not grow into open space, but into serpentine. This is supported by grains belonging to both domains A and B (Fig. 2c, d).

Grain size reduction during faulting by dehydration embrittlement

Two observations suggest that C formed by deformation of B: Firstly, the few large olivine grains in domain C are similar to the olivine in B in that they have abundant magnetite inclusions and a variable forsterite content (Dunkel et al. 2017). Secondly, the small grain size in domain C is caused by deformation of a coarser-grained precursor as shown by the presence of CPO-domains despite a lack of significant crystal-plastic deformation. The sharp contacts between domains B and C, combined with a nearly random distribution of the low-angle misorientation rotation axes in olivine suggest a dominance of brittle deformation. Grain-boundary sliding can also lead to a random distribution of misorientation axes, but is unlikely to have been active at a grain size of 61 μm (average diameter of olivine in domain C). Incipient plastic deformation may have occurred, leading to the patchy subgrains and the weak maxima in the misorientation rotation axes. The shape of olivine CPO-domains in C does not indicate a strong shear movement associated with the grain size reduction. This is supported by the CPO itself, which is similar to that of domains A and B, and would have been significantly modified by shearing. Shear strain was highly localised on the central fault

and smaller branching faults, and not distributed over domain C.

Padrón-Navarta et al. (2010), who also observed grain size reduction associated with deserpentinisation, interpreted it as the result of hydrofracturing due to increasing pore fluid pressure during dehydration of serpentinite. No shear movement was associated with the grain size reduction, which was solely caused by the stress imposed by the pore fluid. In contrast, the displacements associated with deserpentinisation in the LOC show that an anisotropic external stress field affected the dehydrating rocks. Before dehydration, differential stress was insufficient to cause failure. During deserpentinisation, fluid pressure increased, reduced the effective normal stress, and induced dehydration embrittlement (Raleigh and Paterson 1965), which, in the LOC dunites, caused faulting in the vein centres and pulverisation of the surrounding prograde olivine, that is a fragmentation without shearing (Fig. 7d; Dunkel et al. 2017). The survival of the olivine CPO during the dehydration embrittlement and the associated grain size reduction was enabled by a strong strain partitioning in domain C, with localisation of displacement on sharp faults.

An alternative to dehydration embrittlement is collapsing due to the negative volume change during deserpentinisation. However in that case the displacement should scale with the thickness of the dehydrated veins, which it does not (Fig. 1b).

Olivine growth after stress release

In three of the ten analysed veins, the faults did not experience dilation, as evidenced by the chromite layers, which show only displacement parallel to the fault, not perpendicular to it. In the other cases, however, dilation occurred and the inclusion-free olivine of domain D grew. It has low internal misorientations and the subgrains are irregularly shaped, showing that it did not form by deformation, alteration, or recrystallisation of domains A to C, but grew directly from a fluid. How the olivine CPO was transferred from domain C to D is not

clear. Possibly, the olivine in D grew epitaxially on domain C olivine. Epitaxy would influence only the orientation of olivine grains directly at the contact to domain C, and not those further away. This could not be tested, though, because domain D is only two to three grains wide in all analysed samples.

CONCLUSIONS

During dehydration of locally serpentinised dunites from the Leka Ophiolite Complex, Norway, prograde olivine grew on relics of the original mantle olivine present in serpentinite veins. Low nucleation rates and/or effective transport by fluids led to the growth of large olivine grains whose shape was controlled by the distribution of previous microfractures along which serpentinisation had occurred. This produced an unusual, brick-like microstructure in the prograde olivine veins. Dehydration embrittlement caused by the increased fluid pressure during olivine growth led to strain localisation on sharp fault planes and to the fragmentation of the prograde olivine adjacent to the fault.

The CPO of olivine in the host dunite, which developed by crystal-plastic deformation at high temperatures, was preserved in the prograde veins. During initial deserpentinisation, the crystallographic orientation was maintained via the epitaxial growth of prograde olivine on relict primary olivine. During subsequent deformation, the strong strain localisation and the lack of shear strain accompanying the grain size reduction of prograde olivine prevented a significant weakening or modification of the CPO.

The complete preservation of an olivine crystallographic preferred orientation during successive hydration and dehydration may prevent the recognition of these processes in nature. Transient hydration and/or dehydration events can easily be overlooked as the bulk mineralogy hardly changes. Particularly if the degree of serpentinisation was low, detailed microstructural and chemical analyses are necessary to reconstruct the hydration/dehydration

408 evolution.

409 **ACKNOWLEDGEMENTS**

410 This project has been supported by the People Programme (Marie Curie Actions) of
411 the European Union's Seventh Framework Programme FP7/2007-2013/ under REA-Grant
412 Agreement n°608001, 'ABYSS', and by the European Union's Horizon 2020 Research and
413 Innovation Programme under the ERC Advanced Grant Agreement n°669972,
414 'Disequilibrium Metamorphism' ('DIME'), to BJ. The authors thank Fabrice Barou for
415 assistance with the EBSD data acquisition, Christophe Nevado and Doriane Delmas for the
416 high quality thin section polishing, and José Alberto Padrón-Navarta and Julien Gasc for
417 helpful discussions. Comments by Luiz Morales and an anonymous reviewer were greatly
418 appreciated.

419 **REFERENCES**

- 420 Bachmann F, Hielscher R, Schaeben H (2010) Texture analysis with MTEX—free and open
421 source software toolbox. *Solid State Phenomena* 160:63-68
422 doi:10.4028/www.scientific.net/SSP.160.63
- 423 Bachmann F, Hielscher R, Schaeben H (2011) Grain detection from 2d and 3d EBSD data—
424 Specification of the MTEX algorithm. *Ultramicroscopy* 111(12):1720-1733
425 doi:10.1016/j.ultramic.2011.08.002
- 426 Bjerga A, Konopásek J, Pedersen RB (2015) Talc–carbonate alteration of ultramafic rocks
427 within the Leka Ophiolite Complex, Central Norway. *Lithos* 227:21-36
428 doi:10.1016/j.lithos.2015.03.016
- 429 Bons PD, Elburg MA, Gomez-Rivas E (2012) A review of the formation of tectonic veins and
430 their microstructures. *Journal of Structural Geology* 43:33-62

doi:10.1016/j.jsg.2012.07.005

Boudier F, Baronnet A, Mainprice D (2010) Serpentine Mineral Replacements of Natural Olivine and their Seismic Implications: Oceanic Lizardite versus Subduction-Related Antigorite. *Journal of Petrology* 51(1-2):495-512 doi:10.1093/petrology/egp049

Bunge HJ (1982) Texture analysis in materials science : mathematical methods. Butterworths, London doi: 10.13140/RG.2.1.1721.1041

Carter, N.L., Ave'Lallemant, H.G., 1970. High temperature flow of dunite and peridotite. *Geological Society of America Bulletin* 81, 2181-2202. doi: 10.1130/0016-7606(1970)81[2181:HTFODA]2.0.CO;2

Debret B, Andreani M, Godard M, Nicollet C, Schwartz S, Lafay R (2013a) Trace element behavior during serpentinization/de-serpentinization of an eclogitized oceanic lithosphere: A LA-ICPMS study of the Lanzo ultramafic massif (Western Alps). *Chemical Geology* 357(0):117-133 doi: 10.1016/j.chemgeo.2013.08.025

Debret B, Nicollet C, Andreani M, Schwartz S, Godard M (2013b) Three steps of serpentinization in an eclogitized oceanic serpentinization front (Lanzo Massif – Western Alps). *Journal of Metamorphic Geology* 31(2):165-186 doi:10.1111/jmg.12008

Deschamps F, Godard M, Guillot S, Hattori K (2013) Geochemistry of subduction zone serpentinites: A review. *Lithos* 178(0):96-127 doi:10.1016/j.lithos.2013.05.019

Dunkel KG, Austrheim H, Renard F, Cordonnier B, Jamtveit B (2017) Localized slip controlled by dehydration embrittlement of partly serpentinized dunites, Leka Ophiolite Complex, Norway. *Earth and Planetary Science Letters* 463, 277-285. doi:10.1016/j.epsl.2017.01.047

Dungan MA (1977) Metastability in serpentine-olivine equilibria. *American Mineralogist* 62(9-10):1018-1029

455 Dunning GR, Pedersen RB (1988) U/Pb ages of ophiolites and arc-related plutons of the
 456 Norwegian Caledonides: implications for the development of Iapetus. *Contrib Mineral*
 457 *Petrol* 98(1):13-23 doi:10.1007/BF00371904
 458 Fisher, D.M., Brantley, S.L., 1992. Models of quartz overgrowth and vein formation:
 459 Deformation and episodic fluid flow in an ancient subduction zone. *Journal of*
 460 *Geophysical Research: Solid Earth* 97, 20043-20061. doi: 10.1029/92JB01582
 461 Furnes H, Pedersen RB, Stillman CJ (1988) The Leka Ophiolite Complex, central Norwegian
 462 Caledonides: field characteristics and geotectonic significance. *Journal of the Geological*
 463 *Society* 145(3):401-412 doi:10.1144/gsjgs.145.3.0401
 464 Hacker BR, Peacock SM, Abers GA, Holloway SD (2003) Subduction factory 2. Are
 465 intermediate-depth earthquakes in subducting slabs linked to metamorphic dehydration
 466 reactions? *Journal of Geophysical Research: Solid Earth* (1978–2012) 108(B1)
 467 doi:10.1029/2001JB001129
 468 Healy D, Reddy SM, Timms NE, Gray EM, Brovarone AV (2009) Trench-parallel fast axes
 469 of seismic anisotropy due to fluid-filled cracks in subducting slabs. *Earth and Planetary*
 470 *Science Letters* 283(1–4):75-86 doi: 10.1016/j.epsl.2009.03.037
 471 Hielscher R, Schaeber H (2008) A novel pole figure inversion method: specification of the
 472 MTEX algorithm. *Journal of Applied Crystallography* 41(6):1024-1037
 473 doi:10.1107/S0021889808030112
 474 Hyndman RD, Peacock SM (2003) Serpentinization of the forearc mantle. *Earth and*
 475 *Planetary Science Letters* 212(3–4):417-432 doi:10.1016/S0012-821X(03)00263-2
 476 Jabaloy-Sánchez A, Gómez-Pugnaire MT, Padrón-Navarta JA, López Sánchez-Vizcaíno V,
 477 Garrido CJ (2015) Subduction- and exhumation-related structures preserved in
 478 metaserpentinites and associated metasediments from the Nevado-Filábride Complex

479 (Betic Cordillera, SE Spain). *Tectonophysics* 644–645(0):40-57
 480 doi:10.1016/j.tecto.2014.12.022
 481 Jung H, Green Ii HW, Dobrzhinetskaya LF (2004) Intermediate-depth earthquake faulting by
 482 dehydration embrittlement with negative volume change. *Nature* 428(6982):545-549
 483 doi:10.1038/nature02412
 484 Jung H, Katayama I, Jiang Z, Hiraga T, Karato S-I (2006) Effect of water and stress on the
 485 lattice-preferred orientation of olivine. *Tectonophysics* 421(1):1-22
 486 doi:10.1016/j.tecto.2006.02.011
 487 Katayama I, Jung H, Karato S-i (2004) New type of olivine fabric from deformation
 488 experiments at modest water content and low stress. *Geology* 32(12):1045-1048
 489 doi:10.1130/g20805.1
 490 Kay RW (1980) Volcanic Arc Magmas: Implications of a Melting-Mixing Model for Element
 491 Recycling in the Crust-Upper Mantle System. *The Journal of Geology* 88(5):497-522
 492 Lopez-Sanchez, MA, Llana-Fúnez, S (2015) An evaluation of different measures of
 493 dynamically recrystallized grain size for paleopiezometry or paleowattometry studies.
 494 *Solid Earth* 6, 475-495. doi:10.5194/se-6-475-2015
 495 Lopez-Sanchez, MA, (2016) GrainSizeTools script. figshare.
 496 doi:10.6084/m9.figshare.1383130
 497 Mainprice D, Bachmann F, Hielscher R, Schaeber H (2014) Descriptive tools for the analysis
 498 of texture projects with large datasets using MTEX: strength, symmetry and components.
 499 Geological Society, London, Special Publications SP409.8v1 doi: 10.1144/SP409.8
 500 Mainprice D, Silver PG (1993) Interpretation of SKS-waves using samples from the
 501 subcontinental lithosphere. *Physics of the Earth and Planetary Interiors* 78(3):257-280
 502 doi:10.1016/0031-9201(93)90160-B

503 Nicolas A, Christensen NI (1987) Formation of Anisotropy in Upper Mantle Peridotites-A
 504 Review. In: Fuchs K, Froidevaux, C (ed) Composition, structure and dynamics of the
 505 lithosphere-asthenosphere system, American Geophysical Union, Washington, D. C., pp
 506 111-123 doi:10.1029/GD016p0111

507 Padrón-Navarta JA, Tommasi A, Garrido CJ, Sánchez-Vizcaíno VL, Gómez-Pugnaire MT,
 508 Jabaloy A, Vauchez A (2010) Fluid transfer into the wedge controlled by high-pressure
 509 hydrofracturing in the cold top-slab mantle. *Earth and Planetary Science Letters*
 510 297(1):271-286 doi:10.1016/j.epsl.2010.06.029

511 Padrón-Navarta JA, Tommasi A, Garrido C, Mainprice D (2015) On topotaxy and compaction
 512 during antigorite and chlorite dehydration: an experimental and natural study. *Contrib*
 513 *Mineral Petrol* 169(4):1-20 doi:10.1007/s00410-015-1129-4

514 Pedersen, R-B, Johannesen, GM, Boyd, R (1993) Stratiform platinum-group element
 515 mineralizations in the ultramafic cumulates of the Leka ophiolite complex, central
 516 Norway. *Economic Geology* 88:782-803 doi: 10.2113/gsecongeo.88.4.782

517 Plümper O, King HE, Vollmer C, Ramasse Q, Jung H, Austrheim H (2012a) The legacy of
 518 crystal-plastic deformation in olivine: high-diffusivity pathways during serpentinization.
 519 *Contrib Mineral Petrol* 163(4):701-724 doi:10.1007/s00410-011-0695-3

520 Plümper O, Piazzolo S, Austrheim H (2012b) Olivine Pseudomorphs after Serpentinized
 521 Orthopyroxene Record Transient Oceanic Lithospheric Mantle Dehydration (Leka
 522 Ophiolite Complex, Norway). *Journal of Petrology* 53(9):1943-1968
 523 doi:10.1093/petrology/egs039

524 Plümper O, John T, Podladchikov YY, Vrijmoed JC, Scambelluri M (2017) Fluid escape
 525 from subduction zones controlled by channel-forming reactive porosity. *Nature Geosci*
 526 10: 150-156 doi:10.1038/ngeo2865

527 Ramsay JG (1980) The crack-seal mechanism of rock deformation. *Nature* 284(5752):135-
 528 139 doi:10.1038/284135a0

529 Raleigh C, Paterson M (1965) Experimental deformation of serpentinite and its tectonic
 530 implications. *Journal of geophysical Research* 70(16):3965-3985
 531 doi:10.1029/JZ070i016p03965

532 Rutter EH, Llana-Fúnez S, Brodie KH (2009) Dehydration and deformation of intact
 533 cylinders of serpentinite. *Journal of Structural Geology* 31(1):29-43
 534 doi:10.1016/j.jsg.2008.09.008

535 Rüpke LH, Morgan JP, Hort M, Connolly JAD (2004) Serpentine and the subduction zone
 536 water cycle. *Earth and Planetary Science Letters* 223(1–2):17-34
 537 doi:10.1016/j.epsl.2004.04.018

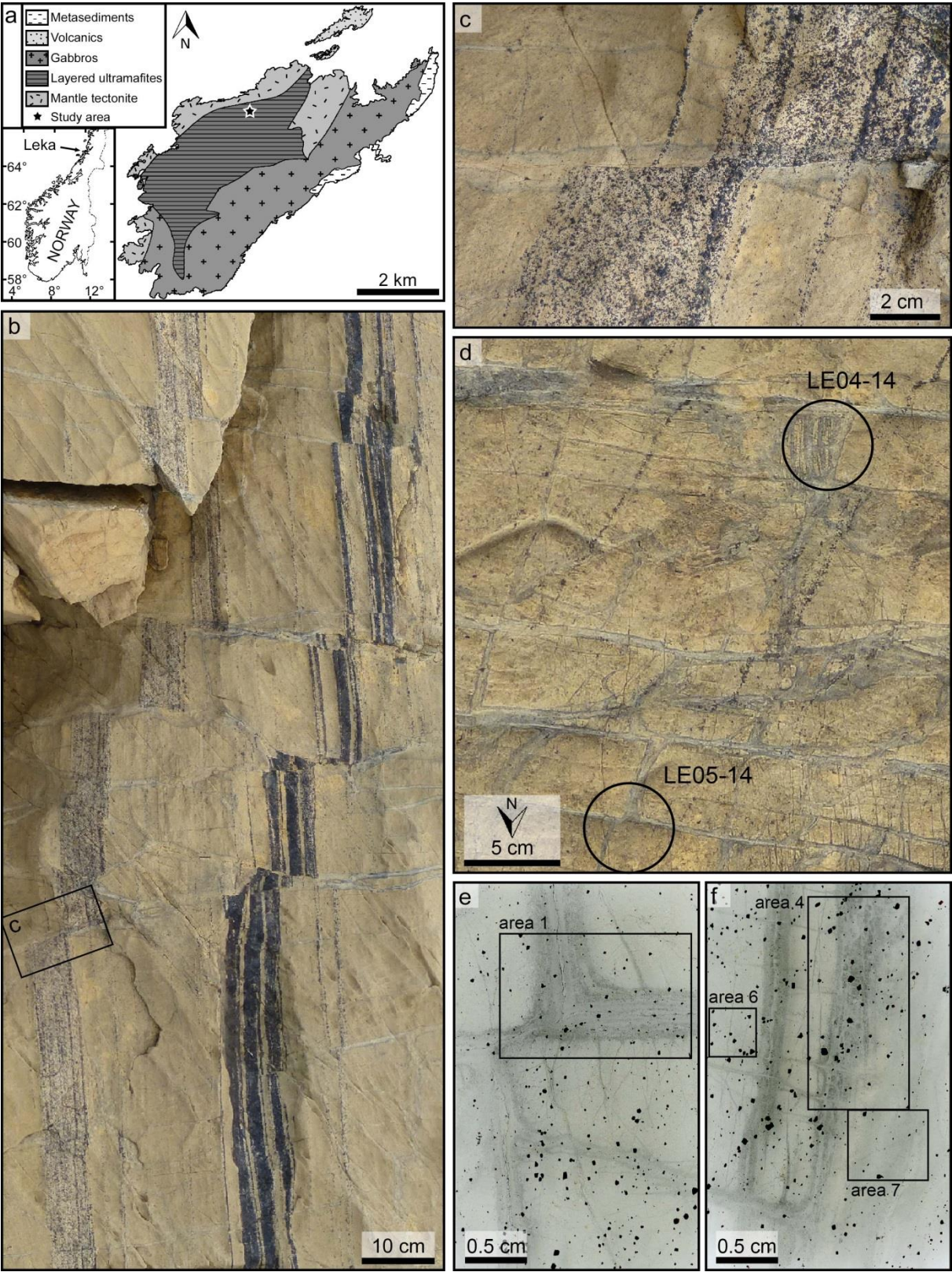
538 Scambelluri M, Strating EH, Piccardo G, Vissers R, Rampone E (1991) Alpine olivine-and
 539 titanian clinohumite-bearing assemblages in the Erro-Tobbio peridotite (Voltri Massif,
 540 NW Italy). *Journal of Metamorphic Geology* 9(1):79-91 doi: 10.1111/j.1525-
 541 1314.1991.tb00505.x

542 Shiina T, Nakajima J, Matsuzawa T (2013) Seismic evidence for high pore pressures in the
 543 oceanic crust: Implications for fluid-related embrittlement. *Geophysical Research Letters*
 544 40(10):2006-2010 doi:10.1002/grl.50468

545 Skemer P, Katayama I, Jiang Z, Karato S-i (2005) The misorientation index: Development of
 546 a new method for calculating the strength of lattice-preferred orientation. *Tectonophysics*
 547 411(1):157-167 doi:10.1016/j.tecto.2005.08.023

548 Snoke AW, Calk LC (1978) Jackstraw-textured talc-olivine rocks, Preston Peak area,
 549 Klamath Mountains, California. *Geological Society of America Bulletin* 89(2):223-230
 550 doi:10.1130/0016-7606(1978)89<223:jtrppa>2.0.co;2

551 Tommasi A, Mainprice D, Canova G, Chastel Y (2000) Viscoplastic self-consistent and
 552 equilibrium-based modeling of olivine lattice preferred orientations: Implications for the
 553 upper mantle seismic anisotropy. *Journal of Geophysical Research: Solid Earth* (1978–
 554 2012) 105(B4):7893-7908 doi:10.1029/1999JB900411
 555 Vance JA, Dungan MA (1977) Formation of peridotites by deserpentinization in the
 556 Darrington and Sultan areas, Cascade Mountains, Washington. *Geological Society of*
 557 *America Bulletin* 88(10):1497-1508 doi:10.1130/0016-
 558 7606(1977)88<1497:fopbdi>2.0.co;2
 559 Yamasaki T, Seno T (2003) Double seismic zone and dehydration embrittlement of the
 560 subducting slab. *Journal of Geophysical Research: Solid Earth* (1978–2012) 108(B4)
 561 doi:10.1029/2002JB001918
 562



564
565 **Fig. 1 a** Geological map of the Leka Ophiolite Complex (after Pedersen et al., 1993), showing

25

566 the location of the study area (WGS84 65.10530, 11.63318) in the layered ultramafites. **b**
567 Sharp displacement of chromite layers (black, vertical) in the centres of prograde olivine
568 veins (grey, horizontal) in dunite (yellow). North is approximately to the top and the outcrop
569 plane is dipping to the west. The diagonal structures in this figure are presumably late features
570 and not discussed in this paper. **c** Detailed view of a vein from **b**. **d** Veins of prograde olivine
571 in dunite, with the locations of the two samples (minicores) selected for this study. Thin
572 chromite layers, defining the magmatic layering, strike approximately NNE-SSW and are
573 displaced along several E-W striking veins. (**e** and **f**) Thinsection scans of samples LE05-14
574 (**e**) and LE04-14(**f**) with the positions of EBSD maps given as black rectangles. The
575 thinsections were made parallel to the outcrop surface, and are oriented in the same way as
576 subfigure **d**. (Thinsection LE04-14 has been imaged from below so that the orientation is the
577 same as that of subfigures **d** and **e**, which is why the orientation map shown in figure 3 is a
578 mirror image.)

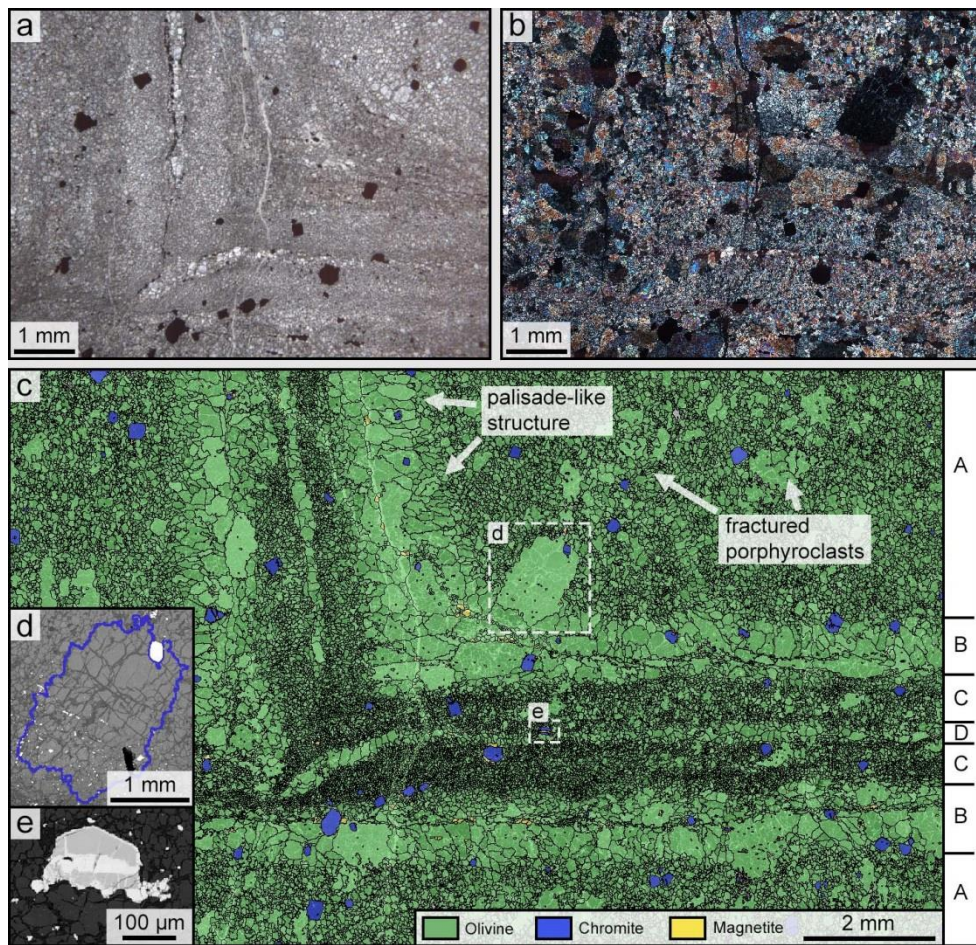


Fig. 2 Vein microstructure of sample LE05-14, area 1 (see Fig. 1e), consisting of olivine and several chromite grains with magnetite rims, shown in optical micrographs with parallel (a) and crossed (b) polarisers and in a phase map overlaid on a band contrast map (c). Some dextral displacement occurred in the horizontal vein. Chromite grains are smeared out in the centre of the vertical vein (a). The faults used to be in the centre of domain C, where domain D grew afterwards. The grains were reconstructed from EBSD mapping. Late low-temperature serpentine (ca. 15 area-%), separating fragments of olivine grains with equal crystallographic orientations, was excluded to reconstruct the olivine microstructures resulting from deserpentinisation. Note the differences in grain size distribution between the domains: Domain A is fine-grained with rare porphyroclasts, domain B coarser, and domain C fine-grained with a more homogeneous grain size than A. A median line might be present in the

middle of domain D in the right part of the horizontal vein. The abundant magnetite inclusions in olivine of domain B are too small to be imaged in the phase map. **d** Backscatter electron (BSE) image of an olivine grain without magnetite inclusions in the part of the grain belonging to domain A (top) and with magnetite inclusions (small white spots) in the part belonging to domain B (bottom). The blue line gives the grain boundary as determined from EBSD analysis. The dark grey mineral fragmenting the olivine is late serpentine, the white grain in the top right chromite. The black spot in the lower right is an artefact. The BSE image was acquired on the Hitachi SU5000 FE-SEM at the Department of Geosciences, University of Oslo. **e** Displaced chromite grain (light grey) in domain C (top) at the border to domain D (bottom), partially altered to ferritchromite and Cr-magnetite (both white).

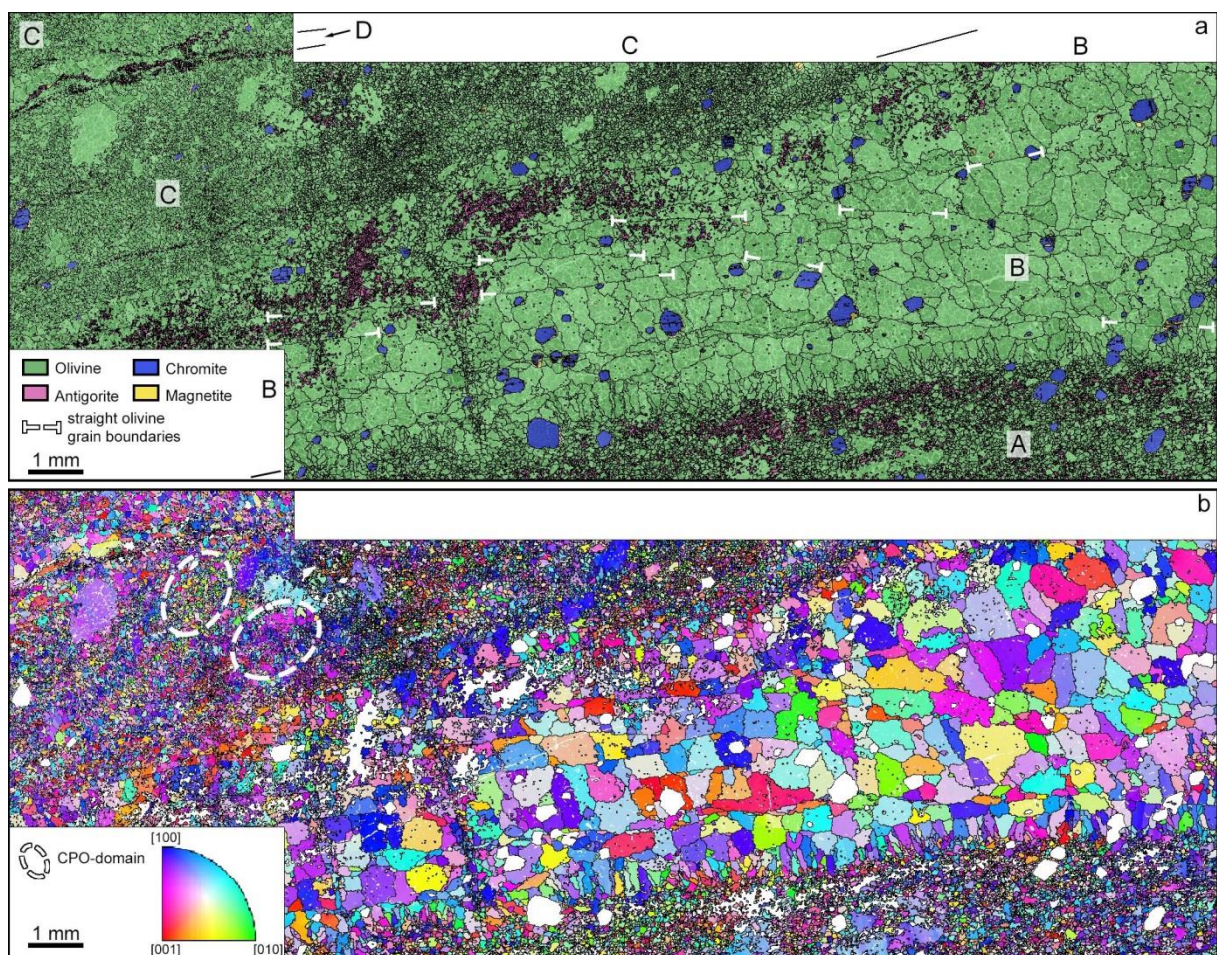


Fig. 3 Vein microstructure and olivine crystallographic orientation of sample LE04-14, areas

4 and 7 (see Fig. 1f). **a** Band contrast map overlaid with phase map. The letters A to D denote the microstructural domains. The small grains within larger olivine grains in domain B are magnetite inclusions. The white markers indicate the positions of straight olivine grain boundaries. Note the palisade-like structure of domain B in contact to domain A. **b** Olivine orientation map with inverse pole figure colour coding. The reference orientation is horizontal. The white ellipses give the position of olivine CPO-domains, indicating a coarser-grained precursor.

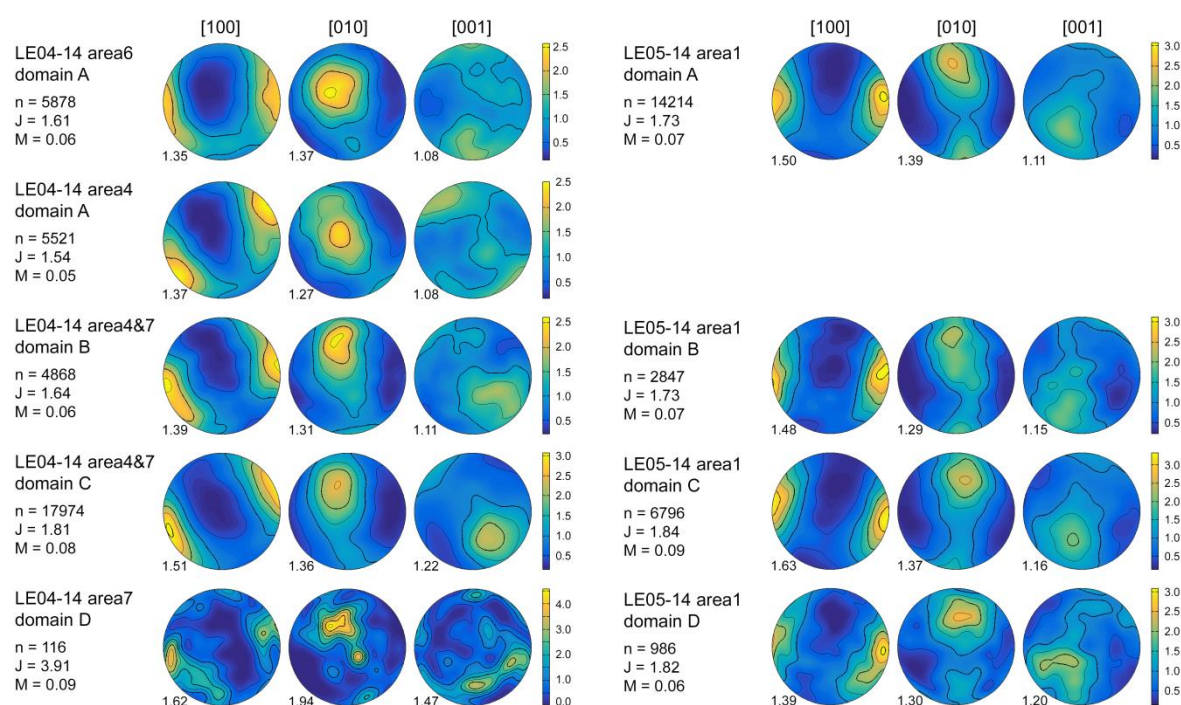


Fig. 4 Lower hemisphere equal-area projections of olivine orientation distribution functions, calculated from average grain orientations. The orientation of the pole figures is perpendicular to the chromite layering and parallel to the thinsection reference frame. Contours are given for multiples of 0.5 of a uniform distribution. n: number of measured grains; J: texture index; M: misorientation index. The numbers to the lower left of the pole figures give the pfJ index (pole figure texture index) of the respective axis. Note that the number of analysed grains is small for domain D.

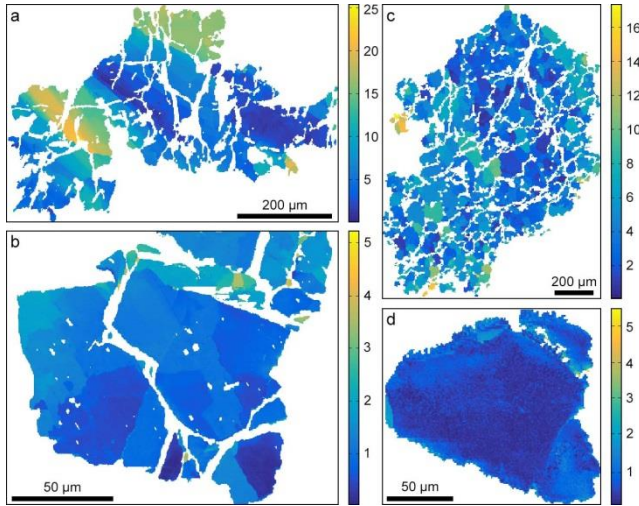


Fig. 5 Internal misorientations in degrees for olivine grains from domains A to D (a-d), relative to the mean orientation of the grain. Note the parallel subgrain boundaries and high misorientations in A and the patchy subgrains in B, C and D. (Sample LE04-14.)

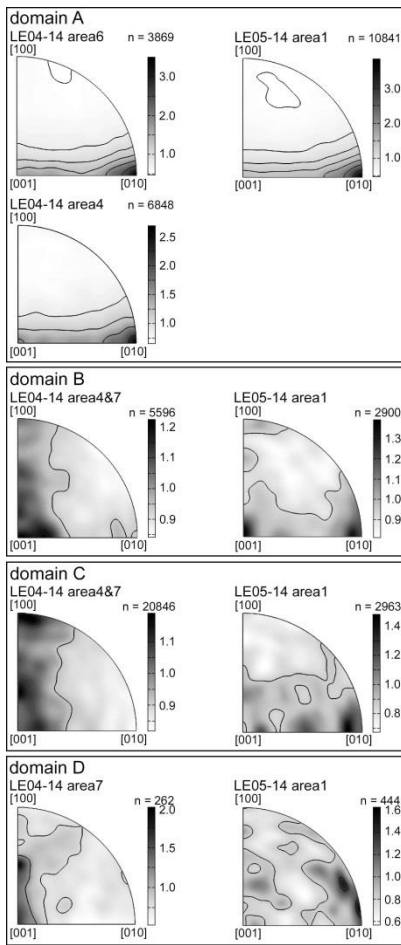


Fig. 6 Orientation of low-angle ($2-10^\circ$) grain-internal misorientation rotation axes in olivine.

Contours are given for multiples of 0.5 of a uniform distribution. Rotation axes are concentrated around [010] and [001] in domain A as opposed to the much weaker distributions in B to D. Note that the number of analysed grains is small for domain D.

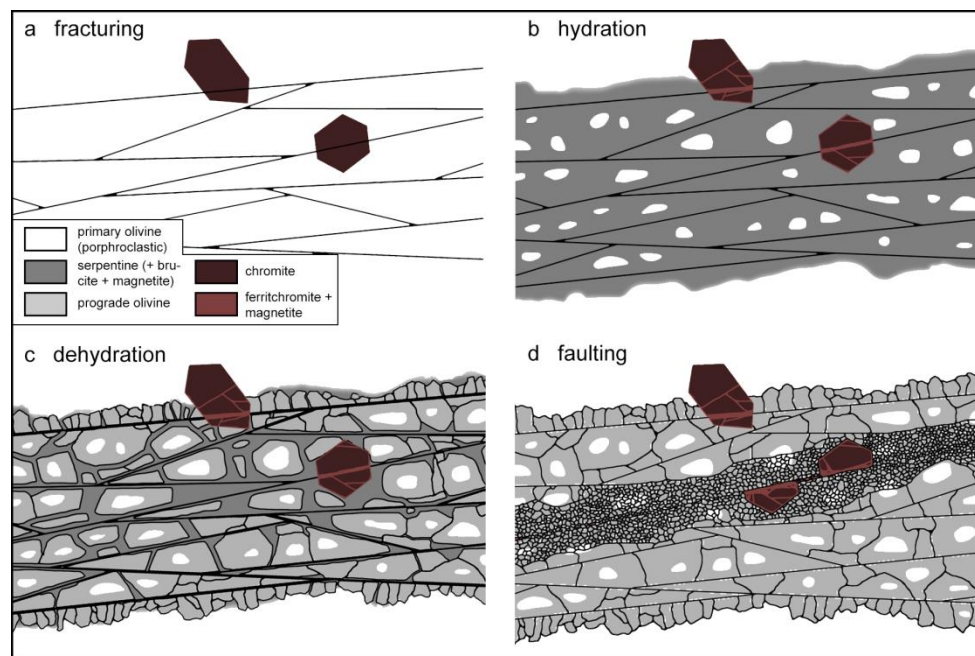
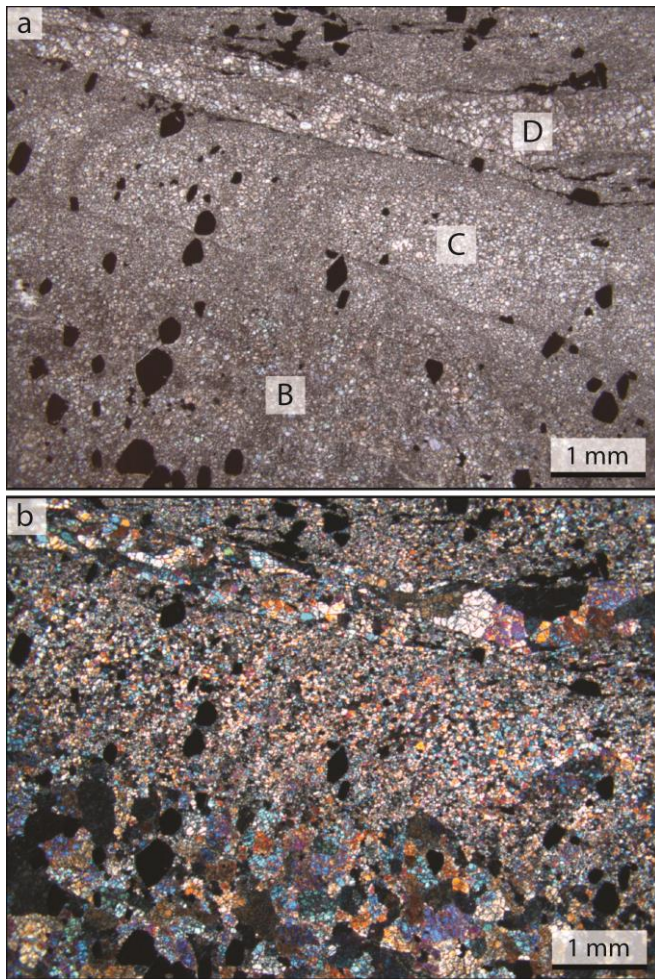


Fig. 7 Microstructural evolution. **a** Fracturing of a porphyroclastic chromite-bearing dunite affected by crystal-plastic deformation (domain A). **b** Hydration of the olivine around the fractures, alteration of chromite. Some relics of primary olivine remain. **c** During dehydration, prograde olivine grows epitaxially on relics of primary olivine (domain B). **d** As dehydration progresses, faulting occurs along the pre-existing serpentine veins, leading to a grain size reduction of the olivine surrounding the fault plane (domain C). Letters denote the microstructural domains.



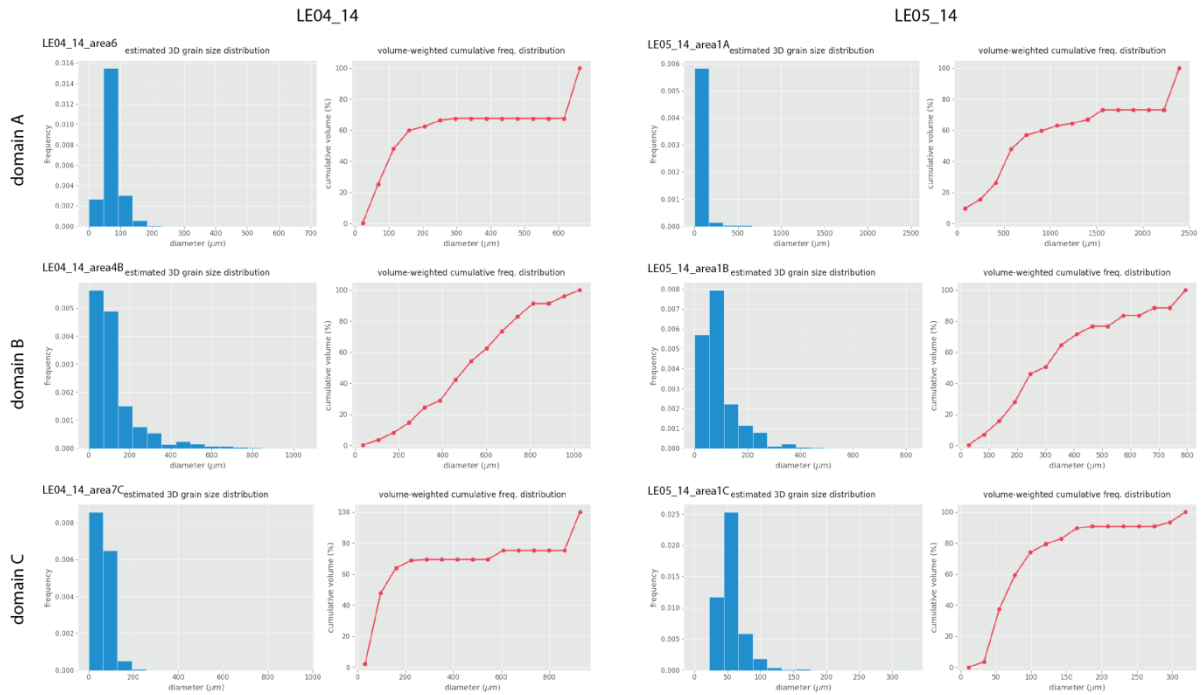
635

636

637

638

Online Resource 1 Optical micrographs taken with plane polarised (a) and cross polarised (b) light showing microstructural domains B, C and D and a displacement of chromite grains in domains C and D.



Online Resource 2 Olivine grain size distributions for domains A to C. Two-dimensional grain sizes were computed from EBSD data using MTEX and the three-dimensional distributions were calculated with the Saltykov method (as described in Lopez-Sanchez and Llana-Fúnez, 2015) using the GrainSizeTools script by Lopez-Sanchez (2016). The steps in the volume-weighted cumulative distribution at high diameters in domains A and C are caused by isolated porphyroclasts (in A) or relict coarse grains (in C) because the measured areas are relatively small.

TABLES

Table 1 Olivine grain sizes. Grain size data from all measured areas has been combined to calculate averages for each domain. Std: standard deviation.

Domain	Equivalent <u>diameter (μm)</u>		Mean equivalent diameter weighted by area (μm)	Number of grains
	mean	std		
A	68	33	119	14749
B	127	124	413	3054
C	61	27	112	11286

Table 2 Olivine fabric intensities, from orientation distribution functions based on one point per grain. J: texture index; M: misorientation index; pfJ: pole figure texture index for each individual axis; min, max: minimum and maximum densities (as multiples of a uniform distribution).

Sample	Domain	Number of grains	J	M	[100]			[010]			[001]		
					pfJ	min	max	pfJ	min	max	pfJ	min	max
LE04-14_area6	A	5878	1.61	0.06	1.35	0.13	2.35	1.37	0.22	2.58	1.08	0.40	1.74
LE04-14_area4	A	5521	1.54	0.05	1.37	0.15	2.50	1.27	0.23	2.35	1.08	0.58	1.79
LE04-14_area4&7	B	4868	1.64	0.06	1.39	0.21	2.61	1.31	0.26	2.58	1.11	0.46	1.86
LE04-14_area4&7	C	17974	1.81	0.08	1.51	0.18	3.06	1.36	0.17	2.52	1.22	0.38	2.31
LE04-14_area7	D	116	3.91	0.09	1.62	0.01	3.74	1.94	0.00	4.78	1.47	0.09	3.39
LE05-14_area1	A	14214	1.73	0.07	1.50	0.17	3.09	1.39	0.15	2.58	1.11	0.46	1.99
LE05-14_area1	B	2847	1.73	0.07	1.48	0.25	3.12	1.29	0.22	2.30	1.15	0.29	1.91
LE05-14_area1	C	6796	1.84	0.09	1.63	0.14	3.33	1.37	0.15	2.56	1.16	0.35	2.05
LE05-14_area1	D	986	1.82	0.06	1.39	0.17	3.09	1.30	0.14	2.61	1.20	0.32	2.16